Peering into the Heart of the Giant Molecular Cloud G148.24+00.41: A Deep Near-infrared View of the Newly Hatched Cluster FSR 655

Vineet Rawat[1,2] ⦿, M. R. Samal[1] ⦿, D. K. Ojha[3] ⦿, Brajesh Kumar[4,5] ⦿, Saurabh Sharma[5] ⦿, J. Jose[6] ⦿, Ram Sagar[7] ⦿, and R. K. Yadav[8] ⦿

[1] Physical Research Laboratory, Navrangpura, Ahmedabad, Gujarat 380009, India
[2] Indian Institute of Technology Gandhinagar Palaj, Gandhinagar 382355, India
[3] Department of Astronomy and Astrophysics, Tata Institute of Fundamental Research, Mumbai 400005, India
[4] South-Western Institute for Astronomy Research, Yunnan University, Kunming, Yunnan, 650500, People's Republic of China
[5] Aryabhatta Research Institute of Observational Sciences, Manora Peak, Nainital 263 002, India
[6] Indian Institute of Science Education and Research (IISER) Tirupati, Rami Reddy Nagar, Karakambadi Road, Tirupati 517 507, India
[7] Indian Institute of Astrophysics, Block II, Koramangala, Bangalore 560034, India
[8] National Astronomical Research Institute of Thailand (NARIT), Sirindhorn AstroPark, 260 Moo 4, T. Donkaew, A. Maerim, Chiangmai 50180, Thailand

Abstract

We present a detailed near-infrared study of an embedded cluster located in the hub of the giant molecular cloud G148.24+00.41 of mass $\sim 10^5 M_\odot$, with the TANSPEC instrument mounted on the 3.6 m Devasthal Optical Telescope. The hub is located near the geometric center of the cloud and represents its most massive clump. We studied the central 2 pc × 2 pc area of the hub with 5σ limiting magnitudes of 20.5, 20.1, and 18.6 mag in the J, H, and K_s bands, respectively. Using the K_s-band luminosity function and comparing it with the synthetic clusters, we obtained the age of the cluster as ~ 0.5 Myr, which was found to corroborate well with the visual extinction versus the age of nearby embedded clusters. We find that the present mass of the cluster is around $\sim 180 M_\odot$, and the cluster is currently forming stars at a rate of $\sim 330 M_\odot \, \mathrm{Myr}^{-1}$, with an efficiency of $\sim 20\%$. The cluster is connected to an extended gas reservoir through a filamentary network; thus, we hypothesize that the cluster has the potential to become a richer cluster in a few Myr of time.

1. Introduction

It is believed that the majority of the stars, if not all, form in a clustered environment. The crowded environment in which stars form determines the properties of stars themselves—the initial mass function (IMF), stellar multiplicity distributions, circumstellar disks, and probably their planetary properties as well.

However, the formation and subsequent evolution of stellar clusters as bound entities remain enigmatic (Lada & Lada 2003; Krumholz et al. 2019). In theories of star cluster formation, it is still debated whether they form monolithically in a single gravitational collapse event or through a hierarchical process involving gas accretion onto protoclusters while stars form concurrently (see reviews by Longmore et al. 2014; Krumholz & McKee 2020; Krause et al. 2020). The flow-driven models, such as global hierarchical collapse (Vázquez-Semadeni et al. 2019) and inertial-inflow model (Padoan et al. 2020) propose that the large-scale converging flows within molecular clouds facilitate the formation of filamentary structures. These structures act like conveyor belts that transport gaseous matter and locally formed stars from the extended environment toward the dense clumps of the hub, which, by accreting matter from the surroundings, will become massive and likely form massive clusters (Vázquez-Semadeni et al. 2017, 2019; Padoan et al. 2020). Observations have identified filament-converging

configurations in clouds, fostering cluster formation at junction points known as hub-filament systems, where matter is found to be funneled via converging flows (Myers 2009; Peretto et al. 2014; Treviño-Morales et al. 2019; Kumar et al. 2020; Ma et al. 2023; Liu et al. 2023).

Although the aforementioned mechanism seems to be a viable way of producing star clusters, the rapid stellar feedback from the newly formed stars can significantly affect the star formation rate (SFR) of the cluster. The feedback from young massive stars can inhibit the gas collapse and isolate the cluster-forming clump from the cloud. The low star formation efficiency (SFE) within the cluster-forming region can also impact the emergence of a rich and bound cluster. Observations and simulations suggest that the embedded phase of star clusters lies somewhere between 1 and 3 Myr depending upon their mass, and bound clusters arise only from regions where SFE is higher than 20%−30% (Lada & Lada 2003; Krumholz et al. 2019). In addition, it is also suggested that the primordial structure and density profile of the gas also play a decisive role in the formation of massive stars and associated clusters (e.g., Bonnell & Bate 2006; Parker et al. 2014; Chen et al. 2021). Thus, the prerequisite condition to improve our understanding of the formation of intermediate to massive star clusters is to investigate a sample of young clusters of different ages and masses that have recently formed in massive clouds. Notably, investigating massive bound clouds featuring hub-filamentary configurations with the hub positioned near the cloud's geometric center is of particular interest. Such clouds offer a likelihood scenario, where the cloud collapses and may form a massive cluster via multiple filamentary flows over an extended period of time.
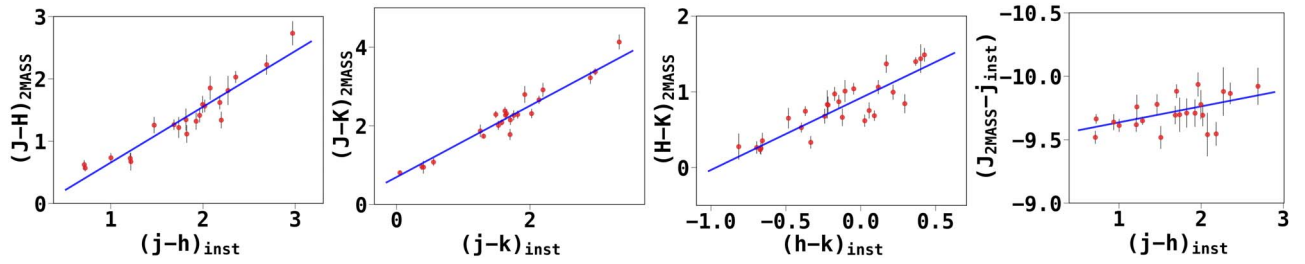
Figure 1. Color–color plots of 2MASS magnitudes vs. TANSPEC instrumental magnitudes in the J, H, and K_s bands.

In a recent work, Rawat et al. (2023) characterized and investigated the massive cloud G148.24+00.41 in order to find out its cluster formation potential and mechanism(s) by which an eventual cluster may emerge. Rawat et al. (2023) found that G148.24+00.41 (distance $\sim$3.4 kpc) is a bound, massive (mass $\sim10^5 M_\odot$), and cold (dust temperature $\sim$14.5 K) giant molecular cloud (GMC) of radius $\sim$26 pc, with a hub-filamentary morphology and it shows the signatures of global hierarchical collapse. Based on CO $(1-0)$ isotopologue observations (spatial resolution $\sim52''$ and velocity resolution $\sim$0.17 km s^{-1}), Rawat et al. (2024b) found that the cloud is host to a massive clump-C1 (i.e., the clump with ID C1 and mass $\sim$2100 $M_\odot$) near its geometric center. They also found that the C1 clump lies at the nexus of several large-scale (14 $-$38 pc) filamentary structures that are combinedly fueling the clump with cold gaseous matter. Using dust continuum observations at 850 μm, Rawat et al. (2024a) further resolved the C1 clump into multiple substructures and found that the central region of the clump, named CC region in their work, is magnetically supercritical with a magnetic field strength of $\sim$24 μG. Using Spitzer near-infrared (NIR) images, Rawat et al. (2023) discussed that a cluster had formed in the clump. This cluster appears to be extremely young, as it is barely visible in optical images, while the clustering of point sources is clearly seen in the Two Micron All Sky Survey (2MASS) and Spitzer images. Froebrich et al. (2007), in their search for embedded clusters using 2MASS images, have identified this cluster as FSR 655. Rawat et al. (2023) found that despite hosting a highly luminous young stellar object (YSO) with a luminosity in the range of 1900$-$4000 $L_\odot$, no radio emission has yet been detected in the clump at 6.7 GHz, implying that an H II region is not yet developed. Thus, the hub is a potential target for understanding the early formation and evolution of a cluster that is embedded in a large reservoir of gas and dust. Despite its importance, so far, no detailed attention has been paid to characterize the cluster based on deep infrared observations. Based on the Spitzer and Wide-field Infrared Survey Explorer catalogs, only a few YSOs have been identified in the literature (Winston et al. 2020). The molecular hydrogen column density (N (H$_2$)) in the direction of the cluster was found to be in the range of $\sim2-3 \times 10^{22}$ cm^{-2} (Rawat et al. 2023), implying a high visual extinction ($A_V \sim 20-30$ mag) for cluster members to be detected in optical and shallow NIR bands (i.e., 10σ limiting sensitivity of $\sim$14.3 mag in K_s band; Skrutskie et al. 2006).

In this work, we conduct a deep NIR analysis of the cluster, using the data obtained with the newly installed 3.6 m Devasthal Optical Telescope (DOT), complemented by catalogs from the Spitzer observations. We aim to improve the understanding of the current status of the cluster in terms of its evolutionary stage, mass distribution, SFE and rate, and likely fate in the context of massive cluster formation. This work is organized as follows: observations, data reduction, and archival data sets are presented in Section 2. The results are presented and discussed in Section 3. In Section 4, we summarize our work with concluding remarks.

2. Observations and Data Sets

2.1. Near-infrared Observations

The NIR photometric observations in the J (1.250 μm), H (1.635 μm), and K_s (2.150 μm) bands were carried out on 2022 November 27 and 29 with the 3.6 m DOT telescope (Sagar et al. 2019, 2020), Nainital, India. The observations were taken using the TIFR-ARIES Near Infrared Spectrometer (TAN-SPEC), mounted at the f/9 Cassegrain focus of the telescope (Sharma et al. 2022). TANSPEC is equipped with a 1k $\times$ 1k HgCdTe imaging array with a pixel scale of 0$''$245, and the image quality is optimized for a $1' \times 1'$ field of view (FOV).

With TANPSEC, we observed the cluster in four pointings, covering $\sim2' \times 2'$ FOV around the central area of the hub. For each pointing, we employed the seven-point dithered pattern in the J, H, and K_s bands. In each dithered position, we took eight frames, with an exposure of 20 s per frame. The total integration time of the observation per pointing was about 19 minutes in the J, H, and K_s bands.

The standard processing tasks of dark correction, flat-fielding, sky subtraction, and bad-pixel masking were performed. For astrometry, we used the WCSTools and SExtractor,[9] and finally obtained the calibrated, stacked, and mosaicked science images in three bands (for details see Ojha et al. 2004; Neichel et al. 2015; Sharma et al. 2023). The FWHM values of the images were in the range of 0$''$8$-$1$''$0.

The photometry was done using the packages available in IRAF (Tody 1986, 1993). Using the DAOFIND task of IRAF, we obtained the list of point sources in the K_s band with signal 5σ above the background. We performed point-spread function photometry of the sources using the ALLSTAR routine of IRAF. For absolute photometric calibration, we used moderately bright and relatively isolated sources from the 2MASS point sources catalog (Skrutskie et al. 2006) with the quality flag "AAA" and photometric error less than 0.1 mag. We obtained the following transformation equations between 2MASS and TANSPEC for the selected sources, which are illustrated in Figure 1.

$$(J - H) = (0.894 \pm 0.069) \times (j - h) - 0.238 \pm 0.131, \tag{1}$$

$$(H - K_s) = (0.950 \pm 0.097) \times (h - k_s) + 0.918 \pm 0.039, \tag{2}$$

$$(J - K_s) = (0.907 \pm 0.036) \times (j - k_s) + 0.696 \pm 0.056, \tag{3}$$

$$(J - j) = (-0.126 \pm 0.040) \times (j - h) - 9.510 \pm 0.055. \tag{4}$$

In the above equations, J, H, and K_s are the standard magnitudes of the stars taken from 2MASS, whereas j, h, and k_s are the instrumental magnitudes from TANSPEC observations. We applied these transformation equations to all the detected sources in the target field. For sources detected in a single band, we simply applied constant shifts to the instrumental magnitudes to get the calibrated magnitudes. These constant shifts were determined in each band as the median difference between the instrumental magnitude and the 2MASS magnitudes for the common sources. In the present work, we consider sources with errors less than 0.2 mag for the analysis. This 5σ sensitivity of the TANSPEC images at the J, H, and K_s bands are found to be 20.5, 20.1, and 18.6 mag, respectively.

2.2. Galactic Population Synthesis Simulation Data

In order to assess the likely contamination of the field population to the cluster population along the line of sight, we obtained the Galactic population in the direction of the cluster using the Besançon population synthesis model[10] (Robin et al. 2004). To obtain the model population, we simulated the Besançon models for an area equivalent to the observed area of the cluster by adopting the 2MASS photometric system and utilizing the atmosphere models grid of Allard & Freytag (2010). In the simulations, we constrained the photometric errors in 2MASS bands by taking the error as an exponentially increasing function of magnitude, as found in our TANSPEC observations for the cluster. The values of the error function parameters fed to the simulations are obtained by fitting the exponential function over the TANSPEC data. For line-of-sight extinction, we used the commonly adopted Galactic extinction value of 1.2 mag kpc^{-1} (Gontcharov 2012). The Besançon model output data contain the distance, visual extinction, J, H, and K_s magnitudes, and spectral type of each synthetic star. We have used this modeled field population to remove the likely contamination present along the line of sight of the cluster (discussed in Section 3.2.2).

2.3. Completeness of the Photometric Data

In order to access the overall completeness limits of the photometric catalogs, we use the histogram turnover method (e.g., Ohlendorf et al. 2013; Samal et al. 2015; Jose et al. 2017; Damian et al. 2021). In this approach, the magnitude at which the histogram deviates from the linear distribution is, in general, considered 90% complete. Figure 2 shows the kernel density estimation (KDE) histograms of the sources detected in various bands. The KDE distribution was done using a multivariate normal kernel, with isotropic bandwidth = 1.2 mag. This value was chosen as we find that it is a good compromise between over- and under-smoothing density fluctuations. With this approach, our photometry is likely to complete down to $J \sim 18.6$ mag, $H \sim 18$ mag, and $K_s \sim 17.7$ mag. We also use the Spitzer 4.5 μm catalog from the GLIMPSE360 survey (Whitney et al. 2008) to access the YSOs of the studied region. The completeness limit of the 4.5 μm
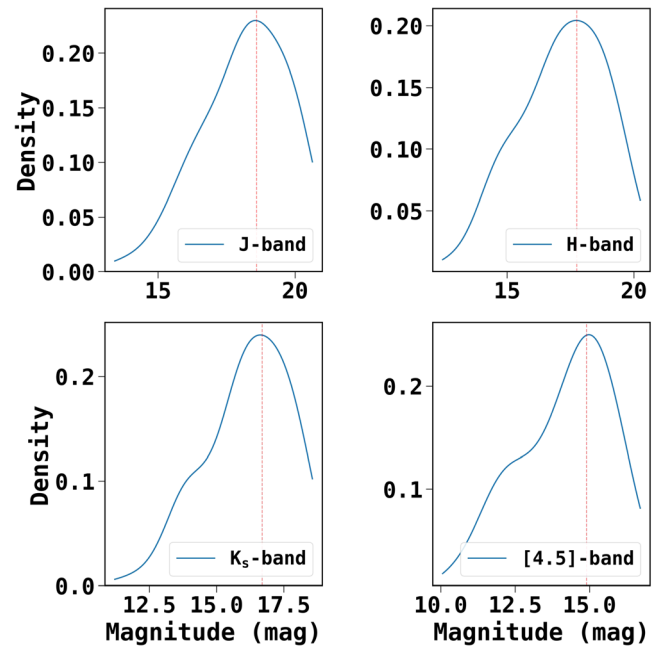
Figure 2. Density plots of photometric data of the cluster region in the J, H, and K_s bands from the TANSPEC and 4.5 μm band from Spitzer. The dashed lines in all the panels show the completeness limiting magnitudes of 18.6 mag, 18 mag, 17.7 mag, and 14.9 mag in the J, H, K_s, and [4.5] μm bands, respectively.

catalog is 14.9 mag and is also shown in Figure 2. The observations were taken as part of the Spitzer Warm Mission Exploration Science program and performed using the two short-wavelength IRAC bands at 3.6 and 4.5 μm.

3. Results and Discussion

3.1. Overview of the G148.24+00.41 in CO

Figure 3(a) shows the distribution of the ^{13}CO integrated emissions of G148.24+00.41 as observed with the Purple Mountain Observatory 13.7 m telescope (beam $\sim$52$''$). Details of the CO observations and the intensity map can be found in Rawat et al. 2024b. The ^{13}CO emission represents the relatively dense inner area of the cloud with an effective radius of $\sim$17 pc (at $d \sim$3.4 kpc). From Figure 3(a), it can be seen that there is a bright spot at the heart of the cloud (i.e., near the geometric center). Based on C^{18}O observations, Rawat et al. 2024b observed that this bright spot corresponds to the location of the most massive clump of the cloud, onto which several large-scale filaments are funneling cold gaseous matter. The small-scale filamentary structures attached to the center of the hub, as found in Rawat et al. 2023, are shown in Figure 3(b), mimicking the hub-filament system morphology as found in other star-forming regions (e.g., Myers 2009; Kumar et al. 2018).

3.2. Stellar Content and Cluster Properties

Figure 3(c) shows the NIR image of the hub as seen in the TANSPEC bands. We find that the clump lacks point sources in the optical bands (e.g., in Digitized Sky Survey's images), while in NIR images, clustering of point sources along with infrared nebulosity can be seen. Figure 4(a) shows the 2D density map of the point sources in the studied area. The stellar density is shown by shaded colors from the peak density to the
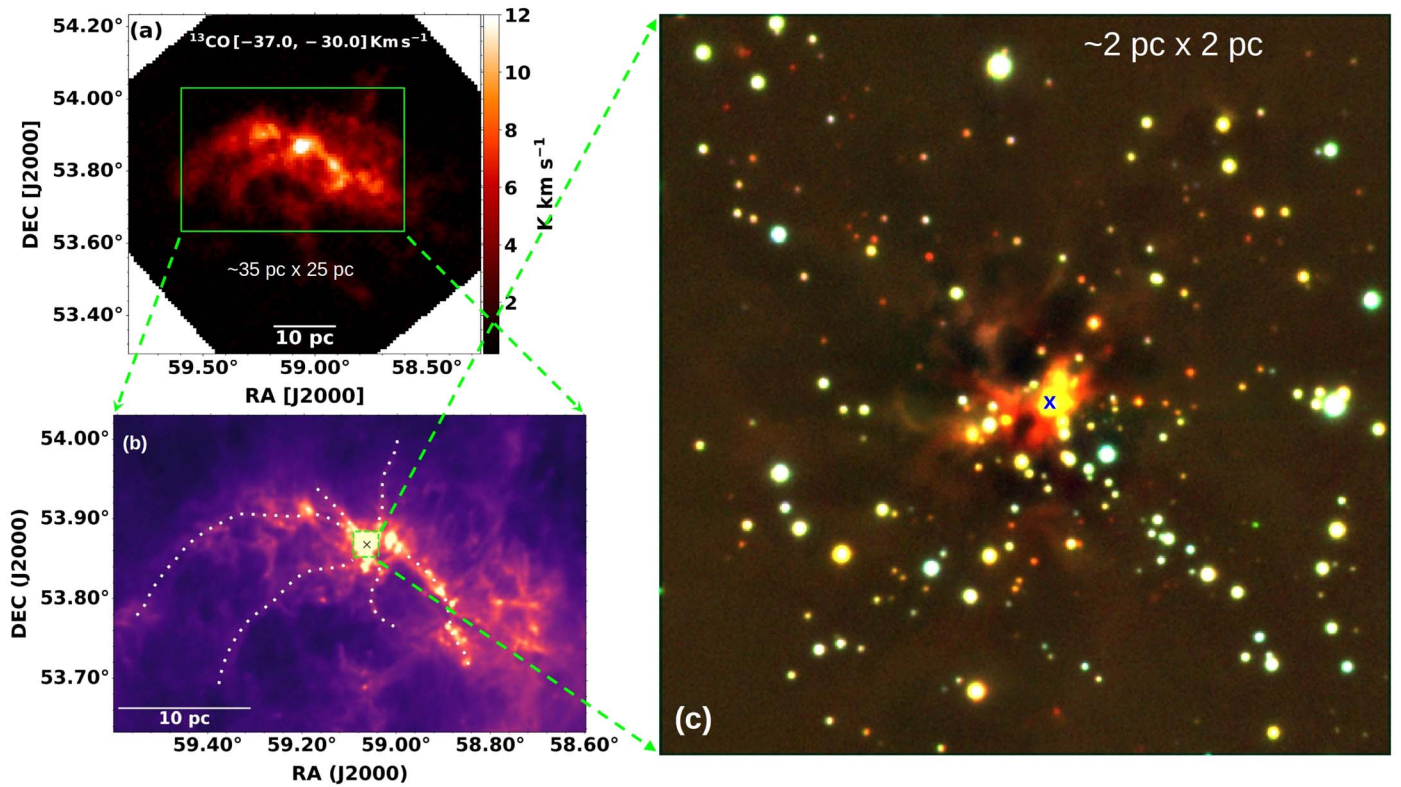
Figure 3. (a) ^{13}CO molecular gas distribution of G148.24+00.41. The green solid box here shows the inner cloud region zoomed-in in panel (b). (b) Herschel 250 μm image of the inner cloud region of size ~35 pc × 25 pc (marked by a green solid box in panel (a)), along with small-scale filamentary structures adopted from Rawat et al. (2023). The green dashed box shows the hub region of size ~2 pc × 2 pc, which is observed with TANSPEC. (c) NIR color-composite image (red: K_s band; green: H band; and blue: J band) of FSR 655 as seen by TANSPEC. The location of the massive YSO (see text) is shown by a cross symbol.

10% level. Figure 4(b) shows the cumulative distribution of stars from the center of the density distribution, and as can be seen, stars are spread within ~90″ radius from the cluster center, with 50% lying within 38″ and 90% within 63″. Beyond 63″, the distribution deviates from the linear shape and becomes flatter, implying that the improvement in the cluster density is insignificant beyond 63″. We thus considered 63″ as the conservative radius of the cluster, which is around 1 pc at the distance of G148.24+00.41 (i.e., ~3.4 kpc).

The cluster is embedded in a cloud of visual extinction as high as 20–30 mag (Rawat et al. 2023), therefore, the contamination due to background stars to the cluster members is expected to be low. Below, we estimate the likely contamination of the field stars and derive properties of the cluster such as the extinction, K_s-band luminosity function, age, mass function, SFE, and SFR.

3.2.1. Extinction

Extinction plays an important role in deriving cluster properties. The line-of-sight extinction of an individual star can be directly determined from knowledge of its color excess and the extinction law. We estimated the extinction of all the stars observed toward the cluster direction within its radius (~1′) using the relation

$$A_V = c \times [(i - j) - (i - j)_0], \qquad (5)$$

where $(i - j)$ is the apparent and $(i - j)_0$ is the intrinsic colors of the point sources in ith and jth filter. Here, c is the constant based on the extinction law of Rieke & Lebofsky (1985), which is 9.34 and 15.98 for the $J - H$ and $H - K_s$ color excess,

respectively. In general, the $H - K_s$ colors are preferred for deriving extinction of star-forming regions (e.g., Gutermuth et al. 2009) because, in such environments, the majority of the sources can be highly embedded in the dust to be detected in the J band. However, excess emission due to circumstellar disks from young sources (see Appendix A for the discussion on the identification of IR-excess sources) can significantly impact the $H - K_s$ colors, causing them to appear redder than their intrinsic photospheric colors, resulting in higher A_V values. This can be significant in young clusters, where a significant fraction of the stars can have a circumstellar disk. We thus used both $J - H$ and $H - K_s$ colors to determine the A_V of the observed sources by assuming that the majority of the sources within the cluster boundary are cluster members. We then made a combined A_V catalog, where priority was given to the A_V values obtained from the $J - H$ colors of the common sources, else A_V values from the $H - K_s$ colors were considered. For estimating A_V, we use the median intrinsic $J - H$ and $H - K_s$ colors of the GKM dwarfs[11] as 0.39 mag and 0.14 mag from Pecaut & Mamajek (2013) as the typical intrinsic color of the point sources. The A_V distribution, with a peak of around 11 mag, is shown in Figure 5. Although some sources show high A_V value, we find that $A_V < 22$ mag encompasses the majority (~90%) of the sources. For sources within $A_V < 22$ mag, we find that the resultant median visual extinction is 11 ± 4 mag, whose corresponding extinction at K_s
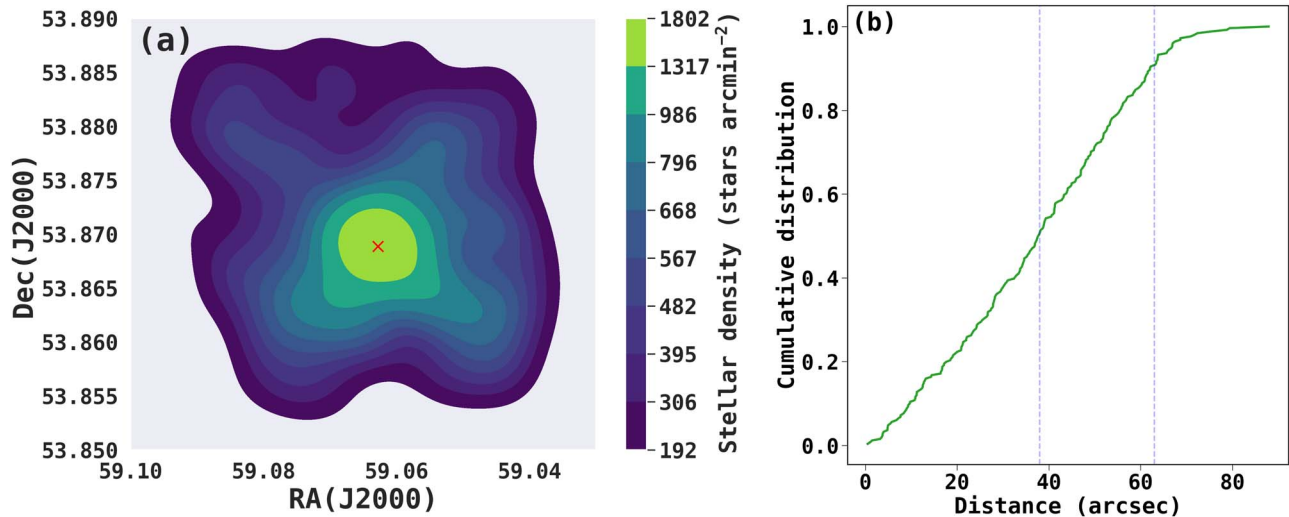
---

[11] Stellar Color/Teff Table

Figure 4. (a) Smoothened 2D density map of the sources, shown from the peak density up to the 10% level of stellar density. (b) Cumulative distribution of all the sources as a function of distance from the cluster center (marked by a cross in panel (a)). The dashed lines show the distances from the cluster center within which 50% and 90% of the sources are lying.
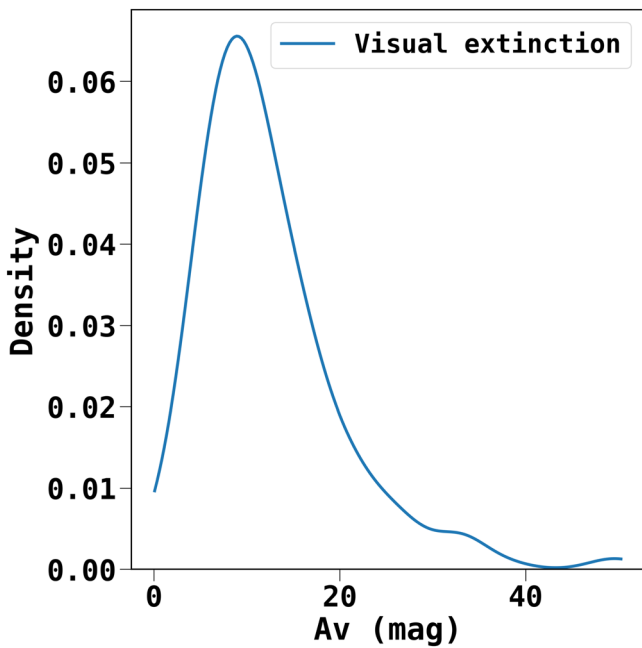

Figure 5. Density plot of all the observed sources in the cluster as a function of their visual extinction (A_V; see Section 3.2.1).

band (A_K) is $\sim 1.23 \pm 0.40$ mag, following the extinction law ($A_K = 0.112 \times A_V$) of Rieke & Lebofsky (1985).

We find that the median A_V for the common sources detected in the H and K_s bands is higher by ~ 1.3 mag compared to the sources detected in the J and H bands. Assuming that the inner-disk emission dominates in the K_s band and has minimal contribution in the H band, we attributed this excess extinction could be due to the emission from the circumstellar disk of the disk-bearing cluster members. This excess extinction is equivalent to $\Delta A_K \sim 0.15$ mag, in the K_s band. We discuss more on this excess extinction in Section 3.2.3.

We acknowledge the fact that although the individual A_V values are derived using the extinction law of Rieke & Lebofsky (1985), they only accurately reflect the true visual

extinctions as long as the assumed reddening law is appropriate for this cloud. The extinction law given by Rieke & Lebofsky (1985) has a negative power-law dependency on the wavelength with a power-law slope, alpha ~ 1.6. Grain growth in cold clouds can alter the extinction law. Some studies show higher alpha values, $1.6-2.6$, with a median around 1.9 in molecular clouds (see Wang & Jiang 2014; Maíz Apellániz 2024, and references therein). If we use the extinction law corresponding to the slope of 1.9 (Messineo et al. 2005), we find that the median A_V of the cluster changes by only ~ 0.3 mag (or $A_K = 0.03$ mag).

In the preceding paragraphs, we determined the median A_V of the cluster by assuming that all the observed sources within the cluster boundary are cluster members. However, if the field population is significant toward the cluster direction, it may affect the true median extinction value of the cluster. To further validate the robustness of the derived extinction value, we use the NIR-excess-emission sources, identified using the JHK_s and $HK_s[4.5]$ color–color (CC) diagrams (discussed in Appendix A) for deriving the median extinction of the cluster. Using only these excess sources (i.e., disk-bearing cluster members) and following the same approach illustrated in the previous paragraphs, we find that the median visual extinction turns out to be around 11 mag, in agreement with the earlier estimation. We also find that using an extinction law of alpha ~ 1.9, the disk fraction remains the same within the error. Since the use of a higher alpha value does not change the results in a major way, we continue further analysis with the extinction law of Rieke & Lebofsky (1985) for the general interstellar medium.

3.2.2. Likely Field Population

Figure 6 shows the $H - K_s$ color distribution of the field sources obtained from the population synthesis model (see Section 2.2), as well as the total observed sources in the cluster direction. As can be seen, the field population shows a narrow $H - K_s$ color distribution peaking at 0.3 mag (i.e., corresponds to $A_V \sim 3$ mag, using Equation (5)), with the majority lying below 0.4 mag (i.e., corresponds to $A_V \sim 4$ mag) while the $H - K_s$ color of the cluster field shows a wide distribution
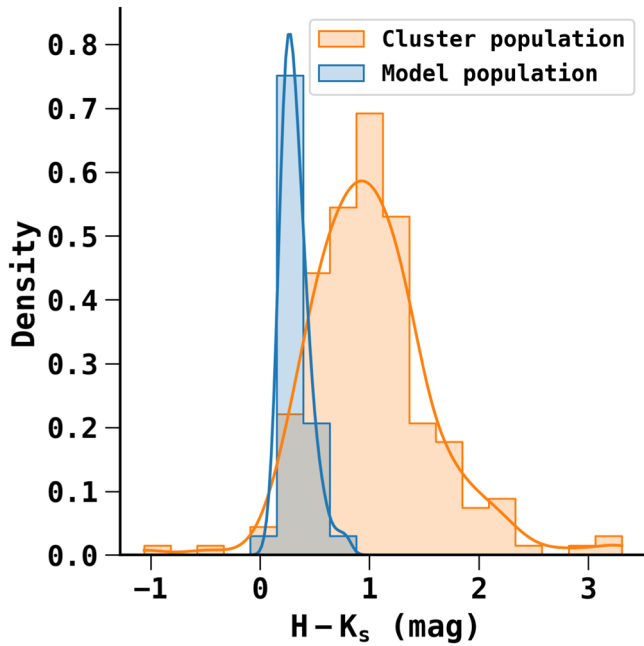
Figure 6. Distribution of all the sources observed toward the cluster and the Besançon model generated sources, shown as a function of their $(H - K_s)$ colors. The blue and orange curves show the corresponding density plots of the cluster and model population, respectively.

having a peak around 1 mag, with the majority lying below 2.5 mag. It implies that the majority of the sources with $H - K_s$ color below $0.4-0.5$ mag are likely the field population along the direction of the cluster. From the population synthesis model, we find that the majority of the model population is located at a distance of less than 3.4 kpc and, thus, is likely the foreground population in the direction of the cluster. There may be some background field stars within our cluster sample, but we assume their contribution to be small, given the sensitivity of our observations and the high column of matter present in the clump. To illustrate this, in Figure 7, we show the K_s versus $H - K_s$ diagram of the population synthesis field sources along with the main-sequence locus reddened by $A_V = 0$, 4, 11, and 22 mag. As can be seen, most of the relatively bright stars (e.g., $K_s < 15.5$ mag) and the majority of the faint stars are located within the $A_V = 4$ mag locus, suggesting 4 mag is likely the foreground extinction in the direction of the cluster. The red stars represent the background sources (i.e., sources with $d > 3.4$ kpc) reddened by $A_V = 11$ mag and $A_V = 22$ mag. As can be seen, if background sources are located behind $A_V = 22$ mag, most of them would be beyond our sensitivity limit of the K_s band, while only a few sources would contaminate our cluster sample if they are located behind the cluster and lie in the range of $A_V \sim 11-22$ mag.

If we assume that most of the sources within the cluster radius with color $H - K_s > 0.5$ mag are likely cluster members, we expect the percentage of background contamination in our sample to be around $\sim 10\%$. We discuss more on this point further in Section 3.2.4. This contamination fraction would be further less if we consider sources above $0.5-1\,M_\odot$. For example, the blue arrow in Figure 7 shows the reddening vector from the base of $1\,M_\odot$ dwarf locus, which reveals that the background contamination above $1\,M_\odot$ is negligible.
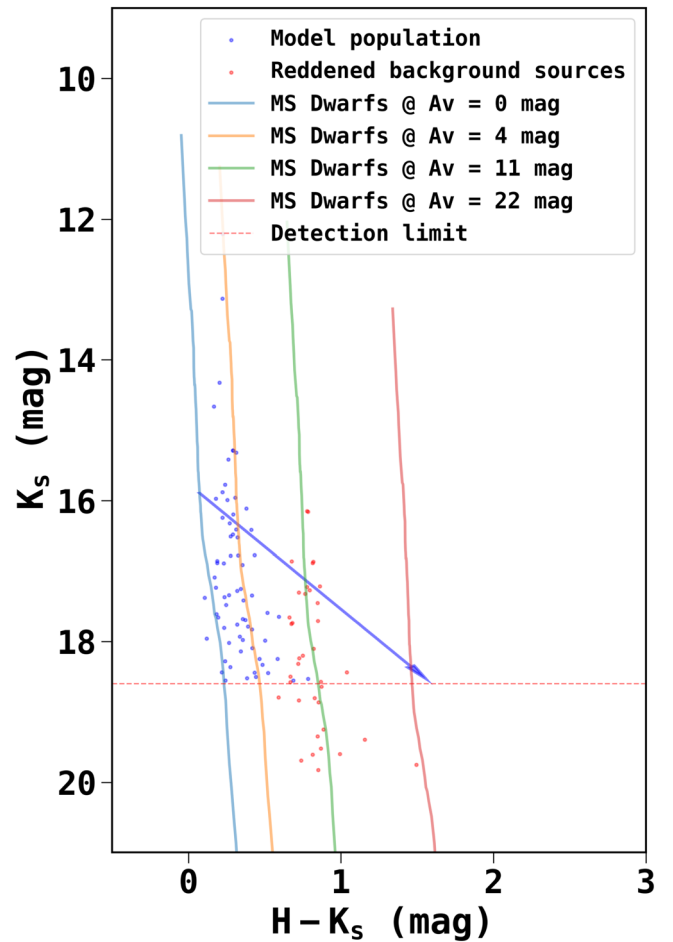

Figure 7. K_s vs. $H - K_s$ diagram of the model population. The red dots show the background sources ($d > 3.4$ kpc) reddened by $A_V = 11$ mag (average extinction toward the cluster). The colored curves show the main-sequence dwarfs locus reddened by $A_V = 0$, 4, 11, and 22 mag. The blue arrow shows the reddening vector drawn from the $1\,M_\odot$ limit.

3.2.3. K_s-band Luminosity Function and Likely Age

The K_s-band luminosity functions (KLFs) of different ages are known to have different peak magnitudes and slopes. Thus, a comparison of the observed KLF with the model KLFs can constrain the age of a cluster (Lada & Lada 1995; Megeath et al. 1996; Muench et al. 2000; Ojha et al. 2004, 2011; Jose et al. 2012; Kumar et al. 2014). KLF is expressed by the following equation:

$$\frac{dN}{dm_k} = \frac{dN}{dM_*} \times \frac{dM_*}{dm_k}, \tag{6}$$

where m_k is the K_s-band luminosity and M_* is the stellar mass (e.g., Lada & Lada 2003). In the equation, the left-hand term represents the number of stars for a given K_s-band magnitude bin, while the first term on the right-hand side is the underlying stellar mass function, and the second term is the mass–luminosity (M–L) relation. To derive the KLF of the cluster, one first needs to correct for field contamination. To do so, we used the model star counts predicted by the Besançon model discussed in Section 2.2. The advantage of using the Besançon model is that the background stars ($d > 3.4$ kpc) can be separated from the foreground stars ($d < 3.4$ kpc). While all the stars in the field suffer a general interstellar extinction, only
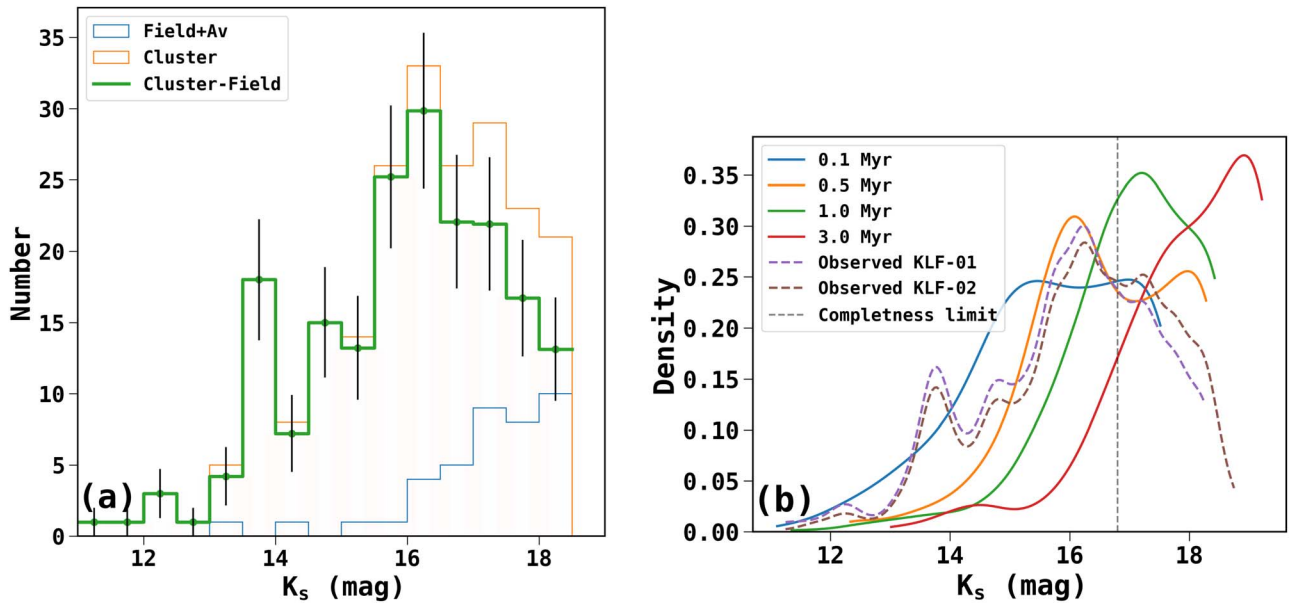
Figure 8. (a) K_s-band luminosity function of the cluster, reddened model control field, and control-field-subtracted cluster shown by orange, blue, and green histograms, respectively. The error bars represent the Poisson error. (b) K_s-band density plots of synthetic clusters of age 0.1, 0.5, 1.0, and 3.0 Myr, shown by solid curves. The dashed curves show the K_s-band density plots of the reddened control-field-subtracted cluster.

the background stars suffer an additional extinction due to the molecular cloud. Besançon model gives extinction of individual stars (A_{Vi}) along the line of sight. The median extinction of the cluster is $A_V = 11$ mag. We, therefore, reddened the background stars by applying an extra extinction of ΔA_{Vi} ($=A_V - A_{Vi}$) to put them behind a cloud of visual extinction 11 mag. We then combined both the foreground and reddened background stars to make a whole set of contaminating field stars. Then, we correct cluster counts by subtracting the contaminating field-star counts from the cluster star counts. The field-corrected cluster KLF, which we called "KLF-01," is shown in Figure 8(a). The figure also shows the KLF of the reddened field and cluster before the field decontamination population. We also made another field-corrected KLF, which we called "KLF-02." The KLF-02 is obtained by simply reddening all the model sources by $A_V = 8$ mag ($A_V = 11 - 3$), thereby bringing both the cluster and field sources to the same median A_V value of 11 mag, and then subtracting the field counts from the cluster counts. The 3 mag is the average extinction of the field sources based on their average $H - K_s$ colors (see Section 3.2.2). The second method is also often adopted in the literature when distance information of the field sources is not available (e.g., Jose et al. 2011).

We then generate synthetic clusters for the age range between 0.1 and 3 Myr at an interval of 0.5 Myr, using the Stellar Population Interface for Stellar Evolution and Atmospheres (SPISEA) Python code (Hosek et al. 2020). We choose the following procedure in the SPISEA code: (1) we assume that the distribution of stars in the cluster follows the Kroupa (2001) mass function, (2) we use the M–L relation for the aforementioned ages from the MIST isochrone models of solar metallicity (Choi et al. 2016), and (3) we adopt the Rieke–Lebofsky extinction laws (Rieke & Lebofsky 1985) and 2MASS filter passbands (for more details, see Hosek et al. 2020). Next, we convert the absolute K_s-band magnitude of the cluster stars to the apparent magnitude using the distance

modulus and average extinction of $A_K \sim 1.2$ mag ($A_V \sim 11$ mag) of the cluster. Then, we construct the KLFs using apparent K_s-band magnitudes and subsequently smooth the KLFs with a Gaussian KDE bandwidth of $K_s = 1$ mag, to account for various uncertainties present in the observed cluster. These uncertainties include the uncertainty of ~ 0.4 mag in the mean extinction of the cluster and a likely uncertainty of ~ 0.15 mag due to excess extinction (see Section 3.2.1), in the K_s band. The last step is done to compare model KLFs with the KLF of the observed cluster. Since SPISEA randomly generates sources for a cluster, we ran the simulation 200 times for each synthetic cluster age. Then we obtain the median KLF for each synthetic cluster. Figure 8(b) shows the model KLFs of different ages along with the observed field-star-subtracted cluster KLFs (KLF-01 and KLF-02) derived in two ways discussed above. As can be seen, barring the bump around $K_s \sim 13.8$ mag, the model KLFs with ages in the range of $0.1 - 1$ Myr appear to be reasonably matching with the observed KLFs, while the overall shape of the observed KLF is in better agreement with the model KLF of age $= 0.5$ Myr. Also, from the disk fraction of FSR 655 (discussed in Appendix B), the age of the cluster seems to be less than a Myr. Therefore, ~ 0.5 Myr appears to be a reasonable assumption as the age of the cluster. The reason for the bump in the KLF around $K_s \sim 13.8$ mag is unclear to us, but we believe that given the small area investigated in this work, the origin of the bump is more of a statistical nature. Wider and deeper observations of the cluster field, as well as a nearby control field, would be able to shed more light on this issue.

In molecular clouds, gas is either consumed in the star formation processes or dissipated by various feedback effects due to forming stellar members. It has been found that molecular clouds with an age greater than ~ 5 Myr are seldom associated with molecular gas (Leisawitz et al. 1989). So, the lack of molecular gas and dust is a proxy indication of the cloud's evolution. In Figure 9, we show the median visual extinction associated with some of the compact (radius < 3 pc) nearby young clusters (< 4 kpc) of age less than 5 Myr that are
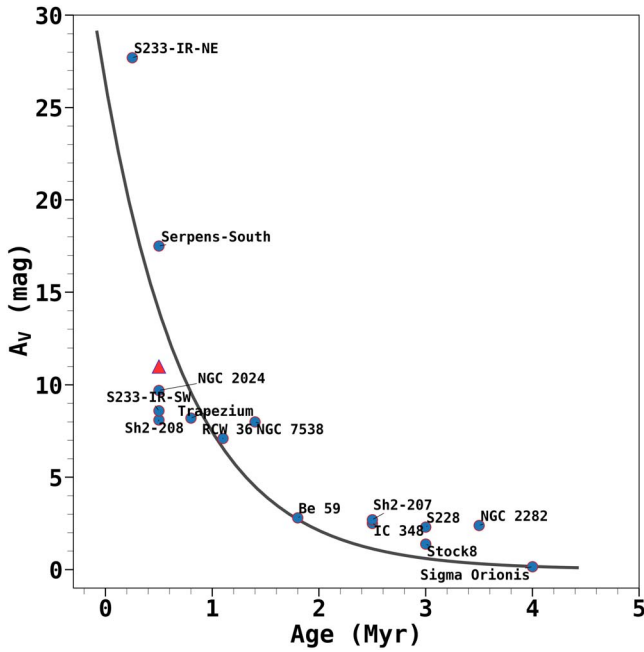
Figure 9. Visual extinction vs. age plot of different nearby clusters ($d \lesssim 4$ kpc), given in Table 1. The black curve shows the best-fit exponential function (see text for details) with fitted parameters, $a \approx 26.30 \pm 3.33$ and $b \approx 1.26 \pm 0.05$. The red triangle shows the position of FSR 655. Here, the extinction values are corrected for foreground extinction, as found in the literature.

Table 1
Parameters of Nearby Clusters

No	Name	A_V (mag)	Age (Myr)	Distance (kpc)	References
1	Stock8	2.0	3.0	2.3	Jose et al. (2017); Damian et al. (2021)
2	Be 59	4.0	1.8	1.0	Panwar et al. (2018)
3	S228	3.3	3.0	3.2	Yadav et al. (2022)
4	IC 348	3.5	2.5	0.32	Muench et al. (2007)
5	Trapezium	9.2	0.8	0.4	Muench et al. (2002)
7	Sh2-208	10.1	0.5	4.0	Yasui et al. (2016a)
8	Sh2-207	2.7	2.5	4.0	Yasui et al. (2016b)
9	S233-IR-SW	9.8	0.5	1.8	Yan et al. (2010)
10	S233-IR-NE	28.9	0.25	1.8	Yan et al. (2010)
11	NGC 2282	4	3.5	1.65	Dutta et al. (2015)
12	NGC 7538	11	1.4	2.7	Sharma et al. (2017)
13	RCW 36	8.1	1.1	0.7	Baba et al. (2004); Ellerbroek et al. (2013)
14	NGC 2024	10.7	0.5	0.42	Levine et al. (2006)
15	Serpens South	19.5	0.5	0.44	Jose et al. (2020)
16	Sigma Orionis	0.155	4.0	0.4	Walter et al. (2008)

Note. The mean extinction values of the clouds are taken from the quoted references. For the age of the regions, wherever the range was given, we have taken the mid values.

associated with a few O-type to early B-type stars (see Table 1). We restrict our sample to the aforementioned type clusters in order to be able to compare with the cluster investigated in this work. As one can see from the figure, the visual extinction is decreasing with the age of the cluster, as expected. Seeing the nature of the plot, we fitted the data points with an exponential decay function of the form, $A_V = a \times \exp(-b\tau)$, where τ is the age of the cluster. Before fitting, the extinction values are first corrected for foreground extinction, as found in the literature. The best-fit values of a and b are $\sim26.30 \pm 3.33$ and $\sim1.26 \pm 0.05$, respectively. We note that though this over-simplified approach suggests a decrease in the column density exponentially with time, the real scenario might be more complex as it strongly depends upon the strength of feedback from the stars present in the clump and the rate of star formation. A better sample with nearly similar cluster mass may provide better results; nonetheless, the obtained result provides a proxy way of seeing how the column density might have evolved in the clumps that are host to low-to-intermediate-mass clusters, like the one investigated in the present work. As can be observed from the figure, the median A_V of FSR 655 is certainly higher than clusters of age older than 2 Myr (e.g., Stock8, IC 348, and S228) and comparable to the extinction of the clusters in the range $0.5-1$ Myr (e.g., NGC 2024, Sh2-208, and S233-IR-SW). This again points to the fact that the studied cluster is unlikely to be older than a Myr. We also found that the disk fraction of the cluster is compatible with other nearby clusters of younger age less than a Myr (for details, see Appendix B).

3.2.4. Mass-extinction-limited Sample

As often adopted in young star-forming regions (Andersen et al. 2011; Luhman et al. 2016), hereafter, we attempted to define a mass-extinction-limited sample of stars to derive

further properties of the cluster. The mass-extinction-limited sample represents all stars in a given area above a certain mass limit after accounting for the effects of extinction and completeness. The primary challenge in obtaining such a sample in young clusters lies in determining the mass limit down to which our data are complete. This determination depends on the age of the cluster and the level of extinction, both of which can be uncertain in young clusters. Unlike open clusters (e.g., Sagar et al. 2001; Sharma et al. 2006; Kumar et al. 2008), young clusters show variable extinction, which makes it difficult to assign a unique mass to a given source. In order to derive the mass-extinction limited sample, we use the H versus $H - K_s$ color–magnitude diagram. Figure 10 shows the H versus $H - K_s$ color–magnitude diagram of all the sources. Assuming that the approximate age of the cluster is around 0.5 Myr, we also show a 0.5 Myr MIST isochrone (Choi et al. 2016) reddened by $A_V = 4$ and 22 mag in Figure 10. In the figure, the completeness limit is also shown by the dashed line, while the reddening vectors originating at masses of $3\,M_\odot$, $2\,M_\odot$, $1\,M_\odot$, and $0.5\,M_\odot$ are shown by blue arrows. To obtain the mass-extinction-limited sample, we choose the visual extinction in the range of $4-22$ mag, because most of the sources below $A_V = 4$ mag are likely the foreground sources of the field, while only 10% of the sources lie above $A_V = 22$ mag. Applying a high extinction threshold would guarantee a complete sample above a certain mass limit, but it would result in a high minimum mass limit above completeness. We find that $A_V = 22$ mag is a reasonable choice to have a statistically significant number of stars while still reaching fairly low masses above the completeness limit. With $A_V = 22$ mag limit, we find that our sample is better complete above $1\,M_\odot$ and considerably complete down to $0.5\,M_\odot$.

Field-star contamination generally dominates in the low-mass ends of the stellar population. We expect the background and foreground contamination levels in our mass-extinction-
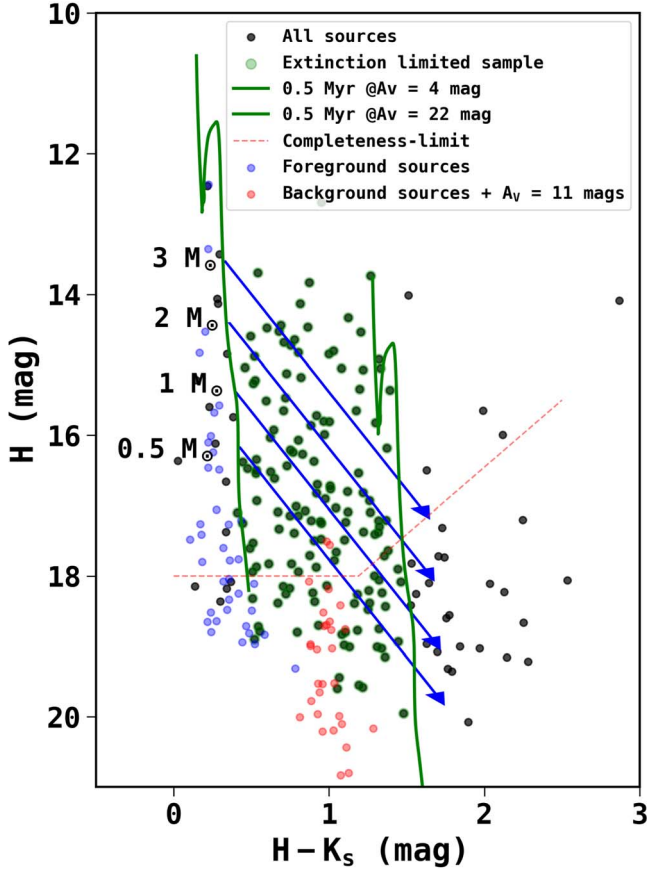
Figure 10. H vs. $H - K_s$ color–magnitude diagram of sources in the cluster and control field. The black dots show all the sources observed in the cluster region. The green dots show the sample within $A_V = 4–22$ mag. The blue dots show the foreground control-field sources, and the red dots show the background control-field sources, which are reddened to match the median visual extinction of the cluster region, i.e., $A_V = 11$ mag. The MIST isochrones of 0.5 Myr (Choi et al. 2016) are reddened by $A_V = 4$ and 22 mag and are shown in green curves. The blue arrows represent the reddening vectors, and the completeness limits of the data are marked by red dashed lines.

limited cluster sample to be minimal. In Figure 10, the foreground (blue dots) and background (red dots) population from the Besançon model are also shown. The background populations are reddened to match the median visual extinction of the cluster, i.e., $A_V = 11$ mag. Even with this minimum extinction, we see almost no background population above $0.5 M_\odot$.

3.2.5. Mass Function

The stellar IMF describes the mass distribution of the stars at birth in a stellar system and is fundamental to several astrophysical concepts. Most of the observational studies focusing on the high-mass end (mass $> 0.5 M_\odot$) have found no gross variation of IMF across the Milky Way disk as well as in the local solar neighborhood (Sagar 2002; Bastian et al. 2010; Hopkins 2018), and are in agreement with Salpeter (Salpeter 1955) or Kroupa (Kroupa 2001)-type mass-function distribution. At the high-mass end (mass $> 0.5 M_\odot$), the mass-function power-law exponent "Γ" is found to be close to 2.3 in the linear form (i.e., $\frac{dN}{dM} \propto M^{-\Gamma}$) or 1.3 in the logarithm form (i.e., $\frac{dN}{d \log M} \propto M^{-\alpha}$; Kroupa 2001), where $\alpha = \Gamma - 1$. Studying young clusters, like the one investigated in this work, has the
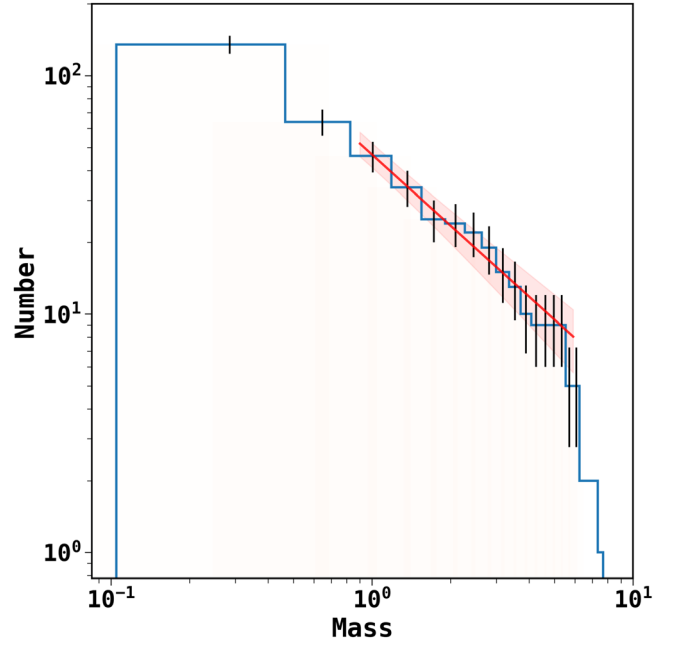

Figure 11. Cumulative initial mass function of the cluster. The red line shows the best-fit power-law mass function with index, $\alpha = 1.00 \pm 0.15$ for the mass range of 1–4 $M_\odot$.

advantage that the dynamical effect of mass segregation will have minimal effect on the shape of the IMF (e.g., Pandey et al. 1992; Allison et al. 2009). In the following, we tried to estimate the IMF of FSR 655.

There are several factors that can affect the IMF shape while dealing with the embedded clusters (e.g., Damian et al. 2021). The principal factors are the effect of NIR-excess and variable extinction in estimating the mass of the stars, low statistics of member stars due to high extinction in getting a robust α value, and contamination at the low-mass end. Since our J band is the least sensitive to the detection of the point sources, to mitigate the effect of NIR-excess sources, we used the H-band luminosity because it is less affected by circumstellar matter, compared to other longer wavelengths. To partially mitigate the effect of low statistics, we use the cumulative mass function of Rodón et al. (2012) of the form:

$$N(>M) \propto kM^{-\alpha}. \tag{7}$$

Figure 11 shows the cumulative mass function, $N(>M)$ of the cluster, where N is the number of sources with mass larger than M and the error bars represent the Poisson noise of $\sqrt{N}$. Using a weighted least-square fit, we find $\alpha = 0.95 \pm 0.12$ for the mass range of 0.5–4 $M_\odot$. By excluding the points lower than 1 $M_\odot$ in the fitting, to avoid any possible bias that may be introduced by the completeness correction and/or in-proper account of field-star contamination at the fainter mass end, we find $\alpha = 1.00 \pm 0.15$ for the mass range of 1–4 $M_\odot$. The obtained slopes are, though flatter, but in agreement with the Kroupa IMF (Kroupa 2001) within 3σ uncertainty, where σ is the error in our measurements. We exclude sources above 4 $M_\odot$ in fitting as the $M–L$ relation at younger ages (e.g., as found with 0.5 Myr MIST isochrone) is nonlinear in the range $4–12 M_\odot$; thus, a star cannot have a unique mass around this mass range. We note that, though our results show a flatter IMF for

FSR 655, but should be treated with caution due to various uncertainties involved.

Future more sensitive photometric and spectroscopic observations would improve the robustness of our results with better estimation of extinction, contamination, and contribution from infrared excess. Nevertheless, the characterization of young compact clusters, like the one investigated in this work, is a useful exercise for assessing the mass distribution at the very initial stages of cluster formation.

3.2.6. Star Formation Efficiency and Rate

The emergence of a bound cluster also depends on the efficiency with which gas is converted into stars, i.e., SFE (ϵ). The SFE is defined as the ratio of the total stellar mass to the total mass of a star-forming region, i.e., stellar mass plus present-day gas mass. We estimate the total gaseous mass (M_{gas}) present in the cluster within its radius. We used the Herschel molecular hydrogen column density map (Marsh et al. 2017) and determined the total integrated column density ($\Sigma N(H_2)$) over the cluster area. We then converted the total column density to mass using the following equation: $M = \mu m_H A_{pix} \Sigma N(H_2)$, where μ is the mean molecular weight taken as 2.8 (Kauffmann et al. 2008), m_H is the mass of the hydrogen atom, and A_{pix} is the pixel area of the column density map in square centimeters at the distance of the cluster. The gas mass of the cluster region is found to be $\sim 750 \pm 337 \, M_\odot$. The uncertainty in the gas mass is around 45%, which includes the uncertainty in the distance of the cloud, gas-to-dust ratio, and dust opacity index (more details of the procedure can be found in Rawat et al. 2023). In order to calculate the mass of the cluster ($M_{cluster}$), we integrated the IMF of the cluster with the Kroupa IMF index, $\Gamma = 2.3$ (Kroupa 2001), within the mass limits of 0.5–15 $M_\odot$. Then, we extrapolated down to 0.08 $M_\odot$ to determine the mass at the lower-mass end, i.e., from 0.5 to 0.08 $M_\odot$, by assuming $\Gamma = 1.3$ (Kroupa 2001). The total stellar mass of the cluster is found to be $\sim 180 \pm 13 \, M_\odot$. Using the M_{gas} and $M_{cluster}$, we calculated the ϵ to be around 0.19 ± 0.07 in the cluster region.

The SFR describes the rate at which the gas in a cloud is converting into stars. The SFR can be estimated as, $SFR = M_{cluster}/t_{sf}$, where t_{sf} is the star formation timescale. Assuming 0.5 Myr as the star formation timescale of the cluster, we obtained the SFR in the cluster region to be around $360 \pm 26 \, M_\odot \, \mathrm{Myr}^{-1}$. The projected area of the cluster region over which we estimated the cloud mass is calculated as πr^2 and is found to be $\sim 3.14 \pm 0.57 \, \mathrm{pc}^2$. Here, $r = 1$ pc is the radius of the cluster region. Normalizing the derived SFR by the cloud area, we got SFR per unit surface area, Σ_{SFR} as $\sim 114.6 \pm 22.2 \, M_\odot \, \mathrm{Myr}^{-1} \, \mathrm{pc}^{-2}$, whereas the gas mass surface density, Σ_{gas} is $\sim 240 \pm 115 \, M_\odot \, \mathrm{pc}^{-2}$.

Krumholz et al. (2012) argued that since different clouds can be at different evolutionary stages, therefore normalizing the Σ_{gas} with the freefall timescale (t_{ff}) would give a better correlation with the Σ_{SFR}. A better correlation of Σ_{SFR} with Σ_{gas}/t_{ff} has been found in some studies (Krumholz et al. 2012; Lee et al. 2016; Pokhrel et al. 2021), and the relation is called the volumetric star formation relation. The general form of the relation is expressed as follows (Krumholz et al. 2012)

$$\Sigma_{SFR} = \epsilon_{ff} \frac{\Sigma_{gas}}{t_{ff}}, \tag{8}$$

where ϵ_{ff} is the SFR per freefall time t_{ff}. Lee et al. (2016) defined the quantity $\epsilon_{ff} = \epsilon \times t_{ff}/t_{sf}$, where ϵ is the SFE of the cluster. To test this star formation relation, we estimate the freefall timescale of the cluster using the following relation

$$t_{ff} = \left(\frac{3 \pi}{32 \, G \mu m_H n_{H_2}} \right)^{1/2}, \tag{9}$$

where n_{H_2} is the gas volume number density of the cluster region, and G is the Gravitational constant. The n_{H_2} is calculated as $M_{gas}/(4/3)\pi r^3 \mu m_H$, which is around $2637 \pm 1318 \, \mathrm{cm}^{-3}$. Using Equation (9), we calculate t_{ff} to be around $\sim 0.60 \pm 0.15$ Myr, and from t_{ff}, $t_{sf} = 0.5$ Myr, and $\epsilon = 0.19$ of the cluster region, we determined ϵ_{ff} to be around 0.23 ± 0.10.

3.2.7. Possibility of FSR 655 Emerging as a Massive Cluster

From the stellar population and gas content of the FSR 655 region, we estimate an SFE of $\sim 19\%$ and SFR of $\sim 360 \, M_\odot \, \mathrm{Myr}^{-1}$ for the cluster. Rawat et al. (2023, 2024b) found that the cluster is located in a massive clump, which is situated at the filamentary hub of the cloud, and the filaments are inflowing cold gaseous matter at a rate of $\sim 675 \, M_\odot \, \mathrm{Myr}^{-1}$ toward the hub. Moreover, Rawat et al. (2024a) found that in the central region of the clump, virial analysis indicates that, at present, the magnetic field and turbulence are not sufficient enough to prevent the collapse of the central clump region. So, we hypothesize that, if the star formation continues in the clump with the current rate for another 2 Myr along with the continuous mass supply through the filaments, then a cluster of total stellar mass $\sim 1000 \, M_\odot$ is expected to emerge at the hub of G148.24+00.41.

4. Summary and Concluding Remarks

In order to better understand the formation of star clusters in GMCs, in this work, we have studied a young cluster, FSR 655 located at the hub of the G148.24+00.41 cloud. To study the cluster properties, we used the TANSPEC NIR camera mounted on the 3.6 m DOT. With TANSPEC, we probe the cluster down to 5σ limiting magnitude of 20.5, 20.1, and 18.6 mag in the J, H, and K_s bands, respectively.

The cluster shows differential extinction with a mean visual extinction of ~ 11 mag, whereas the foreground visual extinction in the direction of the cluster is around 4 mag. The age of the cluster derived by matching the KLF of the cluster members with the KLFs of the synthetic clusters is found to be around 0.5 Myr. Using the JHK_s and HK_s[4.5] CC diagram, we find the disk fraction around $38\% \pm 6\%$ and $57\% \pm 8\%$, respectively.

The mass distribution function of the cluster members agrees with the Kroupa IMF within a 2σ uncertainty, with an α index value of around 1.00 ± 0.15 for the mass range of 1–4 $M_\odot$. Using the Kroupa IMF, we determined the present-day total stellar mass of the FSR 655 cluster to be $\sim 180 \pm 13 \, M_\odot$. The gas mass of the cluster is around $750 \pm 337 \, M_\odot$, which gives an SFE of $\sim 19\% \pm 7\%$ and an SFR of $\sim 360 \pm 26 \, M_\odot \, \mathrm{Myr}^{-1}$.

The robust estimation of all these parameters certainly needed deep high-resolution photometric observations down to the brown-dwarf regime. Nonetheless, taking these results at face value and assuming a constant SFR for a time span of 2 Myr, we find that the cluster has the potential to grow further to become a 1000 $M_\odot$ cluster. In previous studies on G148.24

+00.41 (Rawat et al. 2023), the converging gas flows toward the hub of the cloud that supply the necessary material for star and star cluster formation at the hub have been found. Given the fact that the cluster is located near the geometric center of the cloud, whose mass is $\sim 10^5 \, M_\odot$, and evidence of gas infall onto the region at a high rate via large-scale filamentary flows has been observed, it is not unreasonable to think that the cluster will increase in mass in the future and may emerge as a massive cluster. Moreover, simulation suggests an accelerated pace of star formation in molecular clouds with SFR $\propto t^2$ due to global hierarchical and runway collapse of molecular gas up to a few Myr since the beginning of the star formation (e.g., Caldwell & Chang 2018; Vázquez-Semadeni et al. 2019). So, the possibility of FSR 655 becoming a more massive and richer cluster seems to be viable. Future NIR proper motions and radial velocity observations, in combination with detailed simulations of the stars and gas simultaneously, would be highly desirable to test the above hypothesis for the studied cluster as well as for the embedded clusters in general.

Appendix A
NIR-excess Sources

For deriving cluster properties, the identification of cluster members is crucial. The near and mid-infrared CC diagrams are useful tools to identify the cluster members having NIR-excess emission due to circumstellar disks from young stars. However, other dusty objects along the line of sight may also appear as NIR-excess sources in the CC diagram. Without proper motion or radial velocity information, it is difficult to separate the member sources from the reddened field sources. One possible way to separate the members from the field sources is to compare the CC diagram of the cluster with that of the field sources of the same area and photometric depth. Thus, we made the CC diagrams for the cluster as well as population synthesis model stars and did a comparative analysis of the distribution of the sources. Figures 12(a) and (b) show $J - H$ versus $H - K_s$ CC (*JHKs* CC) diagrams of the cluster as well as model field sources, respectively. In both diagrams, the main-sequence dwarfs' locus is shown by a green curve, and the reddening vector from the location of the M6 dwarf is shown by a blue arrow. In the NIR CC diagram, sources right to the M6 dwarf reddening vector are, in general, considered pre-main-sequence sources with NIR excess (Lada & Adams 1992; Lada & Lada 1995; Haisch et al. 2001).

As can be seen in Figure 12, compared to the cluster region, the NIR-excess zone of the field population is mostly devoid of sources, implying the presence of true NIR-excess sources in the cluster region. From the figure, it can also be noticed that most of the control-field sources are distributed in the CC space of $J - H < 1.0$ mag and $H - K_s < 0.4$ mag. A similar distribution with $J - H$ color less than 1.2 mag can also be seen for a group of sources in the cluster CC diagram. This group seems to be separated from the group of reddened cluster sources in the $J - H$ and $H - K_s$ color space. A comparison of CC diagrams leads us to suggest that the former group of sources in the cluster region is likely the field population along the line of sight. Figures 12(a) and (b) also show the location of the dwarf locus reddened by $A_V = 4$ mag, which fairly matches the distribution of control-field sources and also the likely field population of the cluster region, implying that foreground extinction in front of cluster hosting cloud is around 4 mag. Comparing the CC diagrams, we selected sources with $(J - H)$ color greater than 1.0 mag as NIR-excess sources.
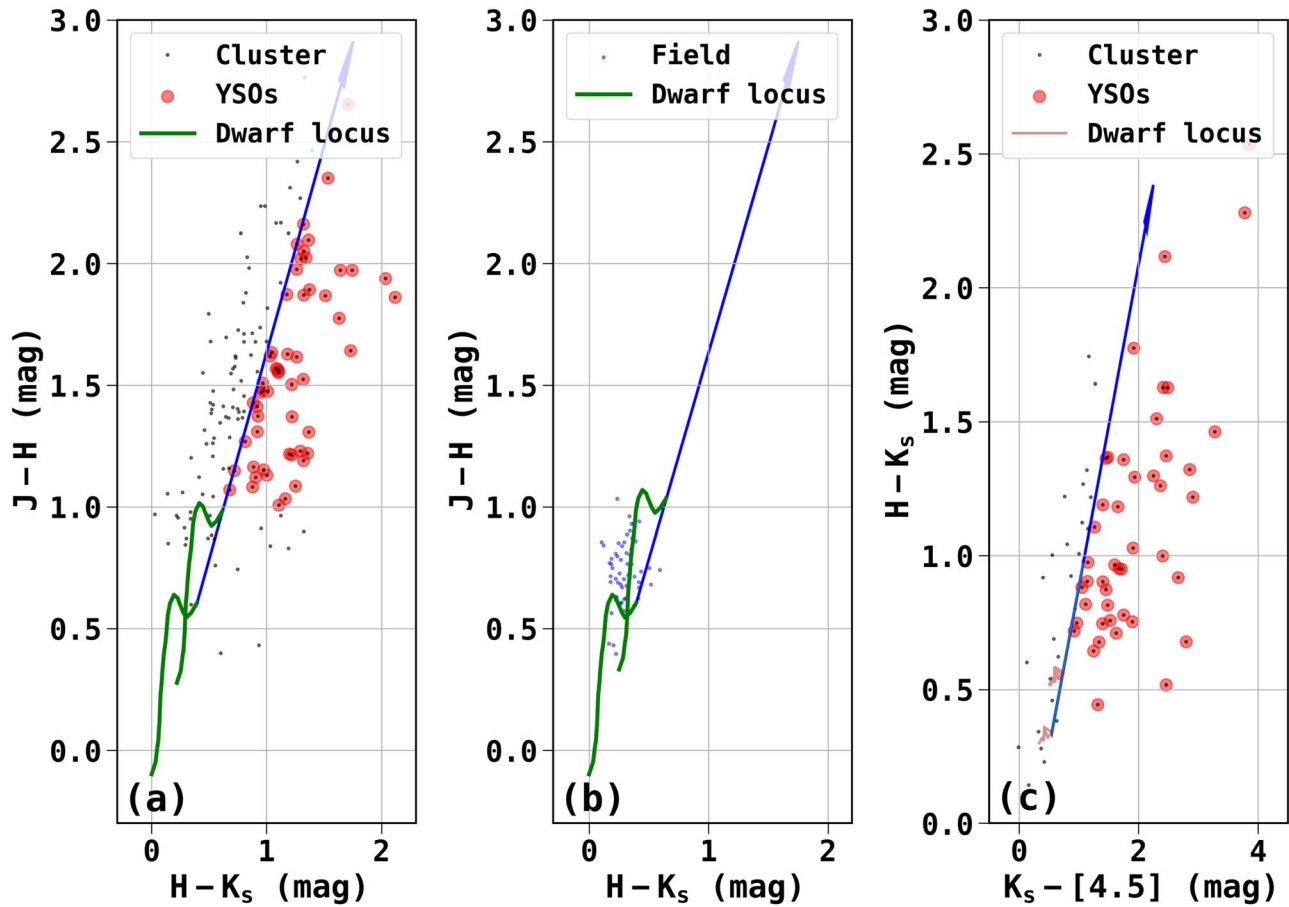
Figure 12. $(J − H, H − K_s)$ CC diagram for the (a) cluster region and (b) modeled control-field region. The green curves are the intrinsic dwarf locus from Bessell & Brett (1988). The blue dots in panel (b) show the modeled field population. (c) $(H − K_s, K−[4.5])$ CC diagram for the cluster region. The brown curves are the intrinsic dwarf locus of late M-type dwarfs (Patten et al. 2006). In panels (a) and (c), the black dots show all the sources observed toward the cluster, and the red dots show the YSOs identified in the cluster, based on their NIR excess in the JHK_s and $HK_s[4.5]$ CC diagrams, respectively. In all the plots, the blue line represents the reddening vector drawn from the location of the M6 dwarf.

It is well known that circumstellar emission from young stars dominates at longer wavelengths, where the spectral energy distribution significantly deviates from the pure photospheric emission. Thus, by incorporating the Spitzer longer wave bands' data into the analysis, a more accurate census of the fraction of stars still surrounded by circumstellar material (i.e., optically thick accretion disks) can be obtained. We thus used the $H − K_s$ versus $K_s − [4.5]$ CC ($HK_s[4.5]$-CC) diagram to identify extra NIR-excess sources (e.g., Samal et al. 2014), which is shown in Figure 12(c). Similar to the JHK_s CC diagram, we selected NIR-excess sources whose $(H − K_s)$ color is greater than 0.5 mag and located right to the reddening vector drawn from the M6 dwarf star.

In summary, with the above approaches, we identified 56 and 47 NIR-excess sources from the JHK_s and $HK_s[4.5]$ CC diagrams, respectively. Including common sources, in total, we identified 82 disk-bearing sources in the cluster region.

Appendix B
Disk Fraction

The disk fraction, which is the frequency of stars with disks within a young cluster, has been widely studied for various star-forming clusters in the solar neighborhood. In general, it has been found that the disk fraction decreases exponentially with the age of the cluster, and the typical lifetime of an optically thick circumstellar disk is around $2−3$ Myr (Haisch et al. 2001).

Using the JHK_s and $HK_s[4.5]$ CC diagrams discussed in Appendix A, we estimate the disk fraction of FSR 655 to be around $47\% \pm 7\%$ and $70\% \pm 8\%$, respectively, where the errors are due to Poisson statistics. However, if we include the photometric error of the cluster members and select only those sources that have excess 1σ (where σ is the color error) above the reddening vector, the disk fraction changes to $\sim38\% \pm 6\%$ and $\sim57\% \pm 8\%$, respectively. To further confirm the disk-bearing cluster members, we determine the Q parameter, $Q = (J − H) − 1.7 \times (H − K_s)$, which gives the deviation from the reddening vector in the JHK_s CC diagram (Comerón et al. 2005; Messineo et al. 2012), following the Rieke & Lebofsky (1985) extinction law. Following the criteria of Comerón et al. (2005), i.e., a star having a Q value of less than $−0.10$ is an NIR-excess source, we estimated the JHK_s disk fraction of FSR 655 to be around 43%. We also find that using a higher alpha value of 1.9 in the extinction law (discussed in Section 3.2.1), the disk fraction of FSR 655 based on Q value estimation changes by only 2%. A similar analysis of Q value for $HK_s[4.5]$ CC-based disk fraction shows comparable results within 1σ uncertainty.

Comparing the disk fractions of FSR 655 with those of the NGC 2024 cluster, which is of similar age ~0.3 Myr (Haisch et al. 2000), we find that the JHK_s and $HK_s[4.5]$ disk fractions
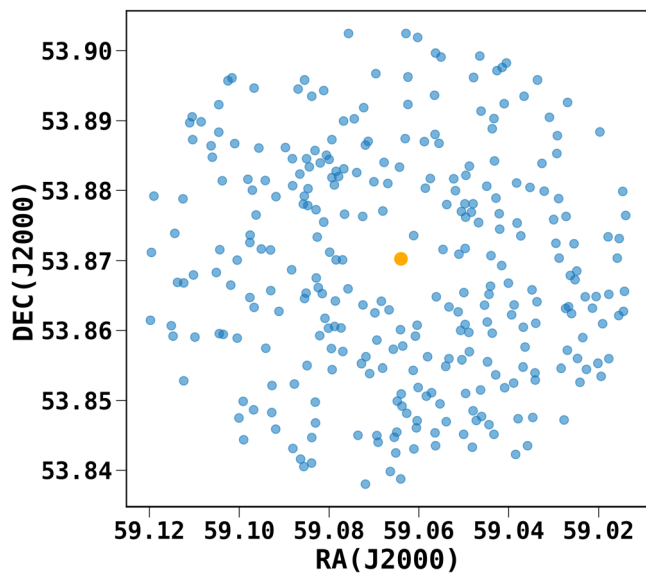
Figure 13. Spatial distribution of the sources visible in the 4.5 μm band, in the cluster direction within a $2'$ radius from the cluster center. The location of the central massive YSO is marked by a yellow dot.

of FSR 655 are comparable to the JHK_s and JHK_sL disk fractions of NGC 2024 (i.e., $\sim58\%$ and $\sim86\%$, respectively) within the limits of uncertainty. However, we want to point out that the $HK_s[4.5]$ CC-based disk fraction estimated for FSR 655, is likely a lower limit. This is due to the presence of a high infrared diffuse background in the vicinity of the cluster center at $3.6\,\mu$m and $4.5\,\mu$m, which can potentially affect the detection of the faint point sources in these bands. This can be readily seen in Figure 13, as a lack of point sources in the vicinity of the central massive star, shown by a yellow dot, compared to the overall distribution of point sources in the area. Deeper and high-contrast observations are required to determine the true JHK_sL or $HK_s[4.5]$ based disk fraction of the cluster.

Furthermore, it has been suggested that the gas and dust in the disk are affected by the stellar radiation of the host stars, thus, the disk fraction also depends on stellar mass. For example, larger disk fractions among lower-mass stars, compared to massive stars, have been found both in simulations (Johnstone et al. 1998; Hollenbach et al. 2000; Pfalzner et al. 2006; Pfalzner & Dincer 2024) and observations (Balog et al. 2007; Kennedy & Kenyon 2009; Stolte et al. 2010; Yasui et al. 2014; Ribas et al. 2015; Damian et al. 2023). It is thus important to estimate the disk fraction in a limited mass range. In this line, Fang et al. 2012 estimated inner-disk fraction based on H, K_s, 3.6, and 4.5 μm data for a number of nearby clusters with stellar members massive than $0.5\,M_\odot$ and found the dependence of disk fraction ($f_{\rm disk}$) on age as $f_{\rm disk} = {\rm e}^{-t/2.3}$, where t is the age in Myr. They also found that for clusters having a higher number of OB stars, the disk dispersal is faster compared to the moderate number of OB stars. We thus estimated disk fraction using the mass-extinction limited sample, which is fairly complete, down to $0.5\,M_\odot$. Doing so, we find the JHK_s CC and $HK_s[4.5]$ CC disk fraction to be around $45\% \pm 7\%$ and $65\% \pm 8\%$. This may be a lower limit considering that our data are not fully complete down to $0.5\,M_\odot$.

Comparing the $HK_s[4.5]$ CC disk fraction of FSR 655 with the samples of Fang et al. (2012; see their Figure 16), we find

that the likely age of the cluster is not more than a Myr. To our knowledge, no disk fraction in the literature has been estimated for cluster members of mass above $0.5\,M_\odot$ using only JHK_s data, so a direct comparison of the JHK_s disk fraction with other clusters is not possible. However, in general, it is comparable to the disk fraction ($\sim50\%-60\%$) of nearby clusters of age $0.5-1$ Myr such as NGC 2024 and ONC (Haisch et al. 2000; Lada et al. 2000), for which disk fraction has been estimated for member stars down to $0.1\,M_\odot$.

ORCID iDs

Vineet Rawat ⬤ https://orcid.org/0000-0001-6515-2863
M. R. Samal ⬤ https://orcid.org/0000-0002-9431-6297
D. K. Ojha ⬤ https://orcid.org/0000-0001-9312-3816
Brajesh Kumar ⬤ https://orcid.org/0000-0001-7225-2475
Saurabh Sharma ⬤ https://orcid.org/0000-0001-5731-3057
J. Jose ⬤ https://orcid.org/0000-0003-4908-4404
Ram Sagar ⬤ https://orcid.org/0000-0003-4973-4745
R. K. Yadav ⬤ https://orcid.org/0000-0002-6740-7425

References

Allard, F., & Freytag, B. 2010, HiA, 15, 756
Allison, R. J., Goodwin, S. P., Parker, R. J., et al. 2009, ApJL, 700, L99
Andersen, M., Meyer, M. R., Robberto, M., Bergeron, L. E., & Reid, N. 2011, A&A, 534, A10
Astropy Collaboration, Price-Whelan, A. M., Sipőcz, B. M., et al. 2018, AJ, 156, 123
Astropy Collaboration, Robitaille, T. P., Tollerud, J. E., et al. 2013, A&A, 558, A33
Baba, D., Nagata, T., Nagayama, T., et al. 2004, ApJ, 614, 818
Balog, Z., Muzerolle, J., Rieke, G. H., et al. 2007, ApJ, 660, 1532
Bastian, N., Covey, K. R., & Meyer, M. R. 2010, ARA&A, 48, 339
Bertin, E., & Arnouts, S. 1996, A&AS, 117, 393
Bessell, M. S., & Brett, J. M. 1988, PASP, 100, 1134
Bonnell, I. A., & Bate, M. R. 2006, MNRAS, 370, 488
Caldwell, S., & Chang, P. 2018, MNRAS, 474, 4818
Chen, Y., Li, H., & Vogelsberger, M. 2021, MNRAS, 502, 6157
Choi, J., Dotter, A., Conroy, C., et al. 2016, ApJ, 823, 102
Comerón, F., Schneider, N., & Russeil, D. 2005, A&A, 433, 955
Damian, B., Jose, J., Biller, B., & Paul, K. T. 2023, JApA, 44, 77
Damian, B., Jose, J., Samal, M. R., et al. 2021, MNRAS, 504, 2557
Dutta, S., Mondal, S., Jose, J., et al. 2015, MNRAS, 454, 3597
Ellerbroek, L. E., Bik, A., Kaper, L., et al. 2013, A&A, 558, A102
Fang, M., van Boekel, R., King, R. R., et al. 2012, A&A, 539, A119
Froebrich, D., Scholz, A., & Raftery, C. L. 2007, MNRAS, 374, 399
Gontcharov, G. A. 2012, AstL, 38, 87
Gutermuth, R. A., Megeath, S. T., Myers, P. C., et al. 2009, ApJS, 184, 18
Haisch, K. E. J., Lada, E. A., & Lada, C. J. 2000, AJ, 120, 1396
Haisch, K. E. J., Lada, E. A., & Lada, C. J. 2001, ApJL, 553, L153
Hollenbach, D. J., Yorke, H. W., & Johnstone, D. 2000, in Protostars and Planets IV, ed. V. Mannings, A. P. Boss, & S. S. Russell (Tucson, AZ: Univ. Arizona Press), 401
Hopkins, A. M. 2018, PASA, 35, e039
Hosek, M. W. J., Lu, J. R., Lam, C. Y., et al. 2020, AJ, 160, 143
Johnstone, D., Hollenbach, D., & Bally, J. 1998, ApJ, 499, 758
Jose, J., Herczeg, G. J., Samal, M. R., Fang, Q., & Panwar, N. 2017, ApJ, 836, 98
Jose, J., Pandey, A. K., Ogura, K., et al. 2011, MNRAS, 411, 2530
Jose, J., Pandey, A. K., Ogura, K., et al. 2012, MNRAS, 424, 2486
Jose, J., Biller, B. A., Albert, L., et al. 2020, ApJ, 892, 122
Kauffmann, J., Bertoldi, F., Bourke, T. L., Evans, N. J., & Lee, C. W, I. 2008, A&A, 487, 993
Kennedy, G. M., & Kenyon, S. J. 2009, ApJ, 695, 1210
Krause, M. G. H., Offner, S. S. R., Charbonnel, C., et al. 2020, SSRv, 216, 64
Kroupa, P. 2001, MNRAS, 322, 231
Krumholz, M. R., Dekel, A., & McKee, C. F. 2012, ApJ, 745, 69
Krumholz, M. R., & McKee, C. F. 2020, MNRAS, 494, 624
Krumholz, M. R., McKee, C. F., & Bland-Hawthorn, J. 2019, ARA&A, 57, 227
Kumar, B., Omar, A., Maheswar, G., et al. 2018, BSRSL, 87, 29

Kumar, B., Sharma, S., Manfroid, J., et al. 2014, A&A, 567, A109
Kumar, B., Sagar, R., & Melnick, J. 2008, MNRAS, 386, 1380
Kumar, M. S. N., Palmeirim, P., Arzoumanian, D., & Inutsuka, S. I. 2020, A&A, 642, A87
Lada, C. J., & Adams, F. C. 1992, ApJ, 393, 278
Lada, C. J., & Lada, E. A. 2003, ARA&A, 41, 57
Lada, C. J., Muench, A. A., Haisch, K. E. J., et al. 2000, AJ, 120, 3162
Lada, E. A., & Lada, C. J. 1995, AJ, 109, 1682
Lee, E. J., Miville-Deschênes, M.-A., & Murray, N. W. 2016, ApJ, 833, 229
Leisawitz, D., Bash, F. N., & Thaddeus, P. 1989, ApJS, 70, 731
Levine, J. L., Steinhauer, A., Elston, R. J., & Lada, E. A. 2006, ApJ, 646, 1215
Liu, H.-L., Tej, A., Liu, T., et al. 2023, MNRAS, 522, 3719
Longmore, S. N., Kruijssen, J. M. D., Bastian, N., et al. 2014, in Protostars and Planets VI, ed. H. Beuther et al. (Tucson, AZ: Univ. Arizona Press), 291
Luhman, K. L., Esplin, T. L., & Loutrel, N. P. 2016, ApJ, 827, 52
Ma, Y., Zhou, J., Esimbek, J., et al. 2023, A&A, 676, A15
Maíz Apellániz, J. 2024, arXiv:2401.01116
Marsh, K. A., Whitworth, A. P., Lomax, O., et al. 2017, MNRAS, 471, 2730
Megeath, S. T., Herter, T., Beichman, C., et al. 1996, A&A, 307, 775
Messineo, M., Habing, H. J., Menten, K. M., et al. 2005, A&A, 435, 575
Messineo, M., Menten, K. M., Churchwell, E., & Habing, H. 2012, A&A, 537, A10
Muench, A. A., Lada, C. J., Luhman, K. L., Muzerolle, J., & Young, E. 2007, AJ, 134, 411
Muench, A. A., Lada, E. A., & Lada, C. J. 2000, ApJ, 533, 358
Muench, A. A., Lada, E. A., Lada, C. J., & Alves, J. 2002, ApJ, 573, 366
Myers, P. C. 2009, ApJ, 700, 1609
Neichel, B., Samal, M. R., Plana, H., et al. 2015, A&A, 576, A110
Ohlendorf, H., Preibisch, T., Gaczkowski, B., et al. 2013, A&A, 552, A14
Ojha, D. K., Samal, M. R., Pandey, A. K., et al. 2011, ApJ, 738, 156
Ojha, D. K., Tamura, M., Nakajima, Y., et al. 2004, ApJ, 616, 1042
Padoan, P., Pan, L., Juvela, M., Haugbølle, T., & Nordlund, Å. 2020, ApJ, 900, 82
Pandey, A. K., Mahra, H. S., & Sagar, R. 1992, BASI, 20, 287
Panwar, N., Pandey, A. K., Samal, M. R., et al. 2018, AJ, 155, 44
Parker, R. J., Wright, N. J., Goodwin, S. P., & Meyer, M. R. 2014, MNRAS, 438, 620
Patten, B. M., Stauffer, J. R., Burrows, A., et al. 2006, ApJ, 651, 502
Pecaut, M. J., & Mamajek, E. E. 2013, ApJS, 208, 9
Peretto, N., Fuller, G. A., André, P., et al. 2014, A&A, 561, A83
Pfalzner, S., & Dincer, F. 2024, ApJ, 963, 122
Pfalzner, S., Olczak, C., & Eckart, A. 2006, A&A, 454, 811
Pokhrel, R., Gutermuth, R. A., Krumholz, M. R., et al. 2021, ApJL, 912, L19
Rawat, V., Samal, M. R., Eswaraiah, C., et al. 2024a, MNRAS, 528, 1460
Rawat, V., Samal, M. R., Walker, D. L., et al. 2023, MNRAS, 521, 2786
Rawat, V., Samal, M. R., Walker, D. L., et al. 2024b, MNRAS, 528, 2199
Ribas, Á., Bouy, H., & Merín, B. 2015, A&A, 576, A52
Rieke, G. H., & Lebofsky, M. J. 1985, ApJ, 288, 618
Robin, A. C., Reylé, C., Derrière, S., & Picaud, S. 2004, A&A, 416, 157
Rodón, J. A., Beuther, H., & Schilke, P. 2012, A&A, 545, A51
Sagar, R. 2002, in IAU Symp. 207, Extragalactic Star Clusters, ed. D. P. Geisler, E. K. Grebel, & D. Minniti (San Francisco, CA: ASP), 515
Sagar, R., Kumar, B., & Omar, A. 2019, CSci, 117, 365
Sagar, R., Kumar, B., & Sharma, S. 2020, JApA, 41, 33
Sagar, R., Munari, U., & de Boer, K. S. 2001, MNRAS, 327, 23
Salpeter, E. E. 1955, ApJ, 121, 161
Samal, M. R., Ojha, D. K., Jose, J., et al. 2015, A&A, 581, A5
Samal, M. R., Zavagno, A., Deharveng, L., et al. 2014, A&A, 566, A122
Sharma, S., Dewangan, L., Panwar, N., et al. 2023, JApA, 44, 46
Sharma, S., Ojha, D. K., Ghosh, A., et al. 2022, PASP, 134, 085002
Sharma, S., Pandey, A. K., Ogura, K., et al. 2006, AJ, 132, 1669
Sharma, S., Pandey, A. K., Ojha, D. K., et al. 2017, MNRAS, 467, 2943
Skrutskie, M. F., Cutri, R. M., Stiening, R., et al. 2006, AJ, 131, 1163
Stolte, A., Morris, M. R., Ghez, A. M., et al. 2010, ApJ, 718, 810
Tody, D. 1986, Proc. SPIE, 627, 733
Tody, D. 1993, in ASP Conf. Ser. 52, Astronomical Data Analysis Software and Systems II, ed. R. J. Hanisch, R. J. V. Brissenden, & J. Barnes (San Francisco, CA: ASP), 173
Treviño-Morales, S. P., Fuente, A., Sánchez-Monge, Á., et al. 2019, A&A, 629, A81
Vázquez-Semadeni, E., González-Samaniego, A., & Colín, P. 2017, MNRAS, 467, 1313
Vázquez-Semadeni, E., Palau, A., Ballesteros-Paredes, J., Gómez, G. C., & Zamora-Avilés, M. 2019, MNRAS, 490, 3061
Walter, F. M., Sherry, W. H., Wolk, S. J., & Adams, N. R. 2008 in Handbook of Star Forming Regions (Vol. I) The Northern Sky ASP Monograph Publicationsed. B. Reipurth, Vol. 4 (San Francisco, CA: ASP), 732
Wang, S., & Jiang, B. W. 2014, ApJL, 788, L12
Whitney, B., Arendt, R., Babler, B., et al. 2008, GLIMPSE360: Completing the Spitzer Galactic Plane Survey, Spitzer Proposal ID, #60020
Winston, E., Hora, J. L., & Tolls, V. 2020, AJ, 160, 68
Yadav, R. K., Samal, M. R., Semenko, E., et al. 2022, ApJ, 926, 16
Yan, C.-H., Minh, Y. C., Wang, S.-Y., Su, Y.-N., & Ginsburg, A. 2010, ApJ, 720, 1
Yasui, C., Kobayashi, N., Saito, M., & Izumi, N. 2016a, AJ, 151, 115
Yasui, C., Kobayashi, N., Tokunaga, A. T., & Saito, M. 2014, MNRAS, 442, 2543
Yasui, C., Kobayashi, N., Tokunaga, A. T., Saito, M., & Izumi, N. 2016b, AJ, 151, 50